

Dryland vegetation pattern dynamics driven by inertial effects and secondary seed dispersal

Giancarlo Consolo^a, Gabriele Grifó^{a,*}, Giovanna Valenti^b

^a Department of Mathematical, Computer, Physical and Earth Sciences, University of Messina (Italy), V.le F. Stagno D'Alcontres 31, I-98166 Messina, Italy

^b Department of Engineering, University of Messina (Italy), C.da di Dio, I-98166 Messina, Italy

ARTICLE INFO

Keywords:

Vegetation stripe patterns
Hyperbolic reaction–advection–diffusion models
Inertial times
Secondary seed dispersal
Wave instability
Travelling wave solutions

ABSTRACT

This manuscript tackles the study of vegetation pattern dynamics driven by inertial effects and secondary seed dispersal. To achieve this goal, an *hyperbolic* extension of the classical *parabolic* Klausmeier model of vegetation, generally used to predict the formation of banded vegetation along the slopes of semiarid environments, has been here considered together with an additional advective term mimicking the downslope motion of seeds. Linear stability analyses have been carried out to inspect the dependence of the wave instability locus on the model parameters, with particular emphasis on the role played by inertial time and seed advection speed. Moreover, periodic travelling wave solutions are taken into account to better characterize modulus and direction of the migration speed of striped vegetation patterns. Theoretical predictions are corroborated by numerical investigations and ecological implications are also discussed. In particular, it is highlighted how the hyperbolic nature of the model may provide possible justifications about some controversial field observations.

1. Introduction

Self-organized patchiness in ecosystems is a clear-cut example of the occurrence of vegetation patterns in water-limited systems (Von Hardenberg et al., 2001; Gilad et al., 2004; Meron, 2015; Zelnik et al., 2017; Meron, 2018; Gowda et al., 2018; Tongway, 2001; Dunkerley, 2018). In particular, regular striped patterns formed along the hillsides of many arid and semi-arid environments are believed to exhibit a non-stationary behaviour which manifests itself as an uphill migration of bands. However, a larger availability of field data has brought out some controversial interpretations about the effective motion of these patches (Tongway, 2001; Dunkerley, 2018). Many mathematical models and numerical tools have been developed to provide a suitable description of the complex phenomena behind the formation, modulation, resilience and propagation of such vegetation patterns (Klausmeier, 1999; Rietkerk et al., 2000; Hillerislambers et al., 2001; Sherratt, 2005; Siteur, 2014; Thompson et al., 2008, 2014; Sohoulane Djebou and Singh, 2015; Thompson and Katul, 2009; Saco et al., 2007; Pueyo et al., 2008; Ursino and Rulli, 2010; Langevelde, 2016; Borgogno et al., 2009; Sherratt and Synodinos, 2012; Sherratt, 2013; Van der Stelt et al., 2013; Eigentler and Sherratt, 2020; Marasco et al., 2014; Gandhi et al., 2018; Bastiaansen et al., 2019). In some previous works (Thompson et al., 2008, 2014; Thompson and Katul, 2009; Saco et al., 2007; Pueyo et al., 2008; Ursino and Rulli, 2010; Langevelde, 2016), the origin of the above-mentioned controversy was

attributed to the phenomena of mobilization, transport and germination of seeds, which can be gathered under the name of *secondary seed dispersal*. It is indeed known that, in sloped terrains, seeds undergo both a primary dispersal from the plant to the ground followed by a secondary dispersal due to their transport in overland flow. This phenomenon has been included in several *parabolic* models (to cite a few, Hillerislambers et al., 2001; Saco et al., 2007; Pueyo et al., 2008; Thompson et al., 2008; Thompson and Katul, 2009 and Consolo and Valenti, 2019). In particular, in the work by our group (Consolo and Valenti, 2019), secondary dispersal of seeds was included in the framework of the Klausmeier model (Klausmeier, 1999) that, as known, is one of the easiest two-compartments models for surface water and vegetation biomass capable of providing a sufficiently adequate description of the formation and movement of vegetation stripes along sloped arid terrains. In that work, much emphasis was given to the role of initial conditions, highlighting how different ecological scenarios can take place when vegetation patterns arise from degradation of homogeneous vegetation or from colonization of bare ground. However, the parabolic nature of the above model prevented the possibility of taking into account those inertial effects which are observed in the vegetation response, in particular for the woody component (Milchunas and Lauenroth, 1995; Garcia-Fayos and Gasque, 2002; Deblauwe et al., 2011; Valentin and d'Herbés, 1999; Deblauwe et al., 2012). It was indeed emphasized that

* Corresponding author.

E-mail address: gabgrifo@unime.it (G. Grifó).

inertia of existing plant populations, namely the tendency to continue residing a given location when the environmental conditions become unfavourable, takes an active role in response to climate change and presence of pollutants. Apart from that, inertial effects can even mask future deteriorations in ecosystem conditions, so constituting more than just a time lag in response to an ongoing stressor.

Accounting for inertia leads to the development of an *hyperbolic* framework that, as known, overcomes the paradox of infinite propagation speed of disturbances and is better suited to describe wave propagation phenomena (Mendez et al., 2010; Zemskov and Horschemke, 2016; Mvogo et al., 2018; Al-Ghoul and Eu, 1996; Hillen, 2002; Straughan, 2011; Curró and Valenti, 2021). The presence of inertia in vegetation dynamics has been considered in some of our previous works (Consolo et al., 2017, 2019, 2020, 2022; Consolo and Grifó, 2022), where it has been emphasized its role both in the transient regime from a spatially-homogeneous steady-state toward a spatially-periodic patterned state and in the modulation of the region of the parameter space in which patterns can be observed. However, to the best of our knowledge, secondary seed dispersal has never been considered in hyperbolic models.

Therefore, the aim of the present work is to inspect how the dynamics of non-stationary vegetation stripes are affected by the simultaneous action of inertial effects and secondary seed dispersal. In detail, in order to characterize the features of the emerging migrating patterns, linear stability analysis has been performed with particular emphasis on the deduction of the threshold condition for wave instability responsible for the onset of oscillatory periodic patterns. Moreover, to gain more insights into the mechanisms underlying the pattern propagation speed, travelling wave solutions have been also taken into account. Analytical predictions have been corroborated by numerical simulations and by a qualitative comparison with some ecological field observations.

The manuscript is organized as follows. The hyperbolic reaction–diffusion–advection model is presented in Section 2 whereas linear stability analyses focused on non-stationary pattern dynamics are addressed in Section 3. Travelling wave solutions are investigated in Section 4 and final remarks are given in Section 5.

2. Model description

Our analysis originates from the classical parabolic version of the Klausmeier model (Klausmeier, 1999), that is one conceptual tool used to mimic striped vegetation dynamics along sloped semi-arid environments. In its original formulation the model describes the spatio-temporal evolution of surface water $w(x, t)$ and vegetation biomass $u(x, t)$ in the presence of an isotropic dispersal of seeds and an anisotropic flow of water through the hillside. Here, water diffusion is neglected since the advection contribution is generally dominant on slopes. Later in Ref. Consolo and Valenti (2019), this model was extended to include the secondary seed dispersal phenomenon and took the 1D dimensionless form:

$$\begin{bmatrix} u \\ w \end{bmatrix}_t - \begin{bmatrix} 1 & 0 \\ 0 & 0 \end{bmatrix} \begin{bmatrix} u \\ w \end{bmatrix}_{xx} - \begin{bmatrix} \psi & 0 \\ 0 & \nu \end{bmatrix} \begin{bmatrix} u \\ w \end{bmatrix}_x = \begin{bmatrix} f(u, w) \\ g(u, w) \end{bmatrix} \quad (1)$$

where the subscript stands for the partial derivative with respect to the indicated variable, the x -axis points along uphill direction and the advection speeds of plant and water are denoted by ψ and ν , respectively. The kinetic functions are given by

$$f(u, w) = wu^2 - Bu, \quad g(u, w) = A - w - wu^2, \quad (2)$$

where A and B are representative of the rates of average annual rainfall and plant loss, respectively. Note that, the original Klausmeier model is recovered for $\psi = 0$.

To account for the presence of biological inertia (Brown et al., 2001; Von Holle et al., 2003; Deblauwe et al., 2011; Garcia-Fayos and Gasque, 2002; Milchunas and Lauenroth, 1995), as well as to provide a better description of pattern propagation, hereafter we consider its hyperbolic

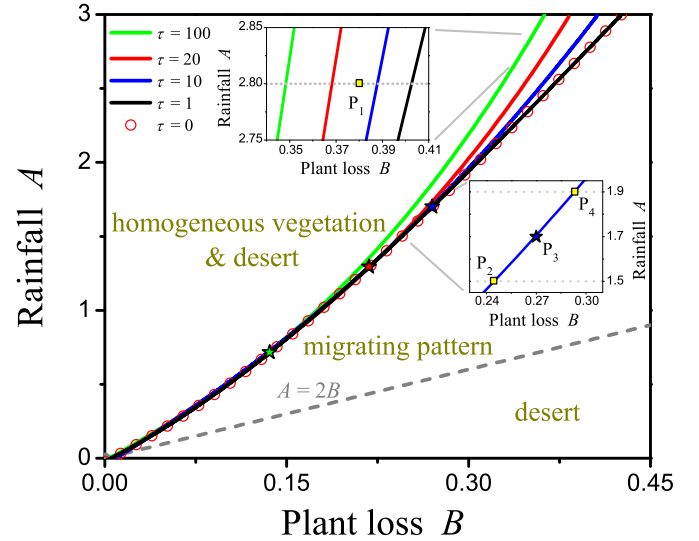


Fig. 1. Solid lines represent the loci of wave instability in the (B, A) parameter plane for different values of inertial time. Red circles denote the locus obtained in the parabolic case. The bottom dashed line defines the condition $A = 2B$, below which only desert state exists. Insets give zooms over the indicated areas. Points P_i ($i = 1, \dots, 4$) represent different configurations in the (B, A) plane which are used in Figs. 2–5. Stars denote Turing bifurcation points obtained as the inertial time is varied.

generalization obtained by means of Extended Thermodynamics (ET) theory (Ruggeri and Sugiyama, 2021; Barbera et al., 2015; Curró and Valenti, 2021). The model reads:

$$\mathbf{U}_t + M\mathbf{U}_x = \mathbf{N}(\mathbf{U}), \quad (3)$$

with

$$\mathbf{U} = \begin{bmatrix} u \\ w \\ J \end{bmatrix}, \quad M = \begin{bmatrix} -\psi & 0 & 1 \\ 0 & -\nu & 0 \\ \frac{1}{\tau} & 0 & 0 \end{bmatrix}, \quad \mathbf{N}(\mathbf{U}) = \begin{bmatrix} f(u, w) \\ g(u, w) \\ -\frac{1}{\tau}J \end{bmatrix} \quad (4)$$

being τ and $J(x, t)$ the inertial time and the dissipative flux, respectively, associated to plant evolution. According to ET theory, the flux is considered as an additional state variable satisfying a thermodynamically-consistent balance law, $\tau J_t + u_x = -J$, that reduces to the classical gradient-based Fick's law for vanishing inertial time $\tau \rightarrow 0$. Readers interested in the full derivation of the hyperbolic model may refer to Ref. Barbera et al. (2015).

It is known that, for $A > 2B$ the model (3), (4), with $f(u, w)$ and $g(u, w)$ given by (2), admits three distinct spatially-homogeneous steady states \mathbf{U}^* given by:

$$\begin{aligned} \mathbf{U}_D^* &= (0, A, 0) \\ \mathbf{U}_L^* &= (u_L, B/u_L, 0) \\ \mathbf{U}_S^* &= (u_S, B/u_S, 0) \end{aligned} \quad (5)$$

where:

$$u_L = \frac{A - \sqrt{A^2 - 4B^2}}{2B}, \quad u_S = \frac{A + \sqrt{A^2 - 4B^2}}{2B}, \quad 0 < u_L < 1 < u_S. \quad (6)$$

From an ecological viewpoint, the first state \mathbf{U}_D^* is representative of the desert state whereas the other ones of uniformly-vegetated areas. Note that, for $A < 2B$ the desert state is the only admitted one, whereas $\mathbf{U}_L^* \equiv \mathbf{U}_S^*$ for $A = 2B$. According to literature, realistic values of rainfall and plant loss belong to the ranges $B \in (0, 2)$ and $A \in (0, 3)$ (Rietkerk, 2002; Klausmeier, 1999; Sherratt, 2010). Moreover, water advection speed is generally taken as $\nu \lesssim 200$ (Klausmeier, 1999) whereas, since secondary seed dispersal represents a small percentage of the former mechanism, it is realistic to assume $\psi \ll \nu$ (Consolo and Valenti, 2019).

3. Wave bifurcation analysis

In order to investigate the nature of the steady states (5), a linear stability analysis for the PDE system (3), (4) is now carried out. Due to its high variability given by natural, human and herbivory effects, the plant loss B is considered as the control parameter. Then, by perturbing the steady state, namely by looking for solutions in the form of $U = U^* + \hat{U} \exp(\omega t + i k x)$, we get

$$(\omega I + ikM - (\nabla N)^*) \hat{U} = 0 \tag{7}$$

where I denotes the identity matrix, $\nabla \equiv \partial/\partial U$ represents the gradient with respect to the field variables and the asterisk indicates the evaluation at U^* . Searching non-trivial solutions of (7) leads to the following characteristic equation:

$$\tau \omega^3 + [A_1 - ik\tau(\nu + \psi)] \omega^2 + \{A_2 + ik[\tau(\nu f_u^* + \psi g_w^*) - (\nu + \psi)]\} \omega + A_3 + ik[\nu f_u^* + \psi g_w^* - \nu k^2] = 0 \tag{8}$$

where

$$\begin{aligned} A_1 &= 1 - \tau(f_u^* + g_w^*) \\ A_2 &= \hat{A}_2 k^2 + \tilde{A}_2 \\ \hat{A}_2 &= 1 - \tau\nu\psi \\ \tilde{A}_2 &= \tau(f_u^* g_w^* - g_u^* f_w^*) - (f_u^* + g_w^*) \\ A_3 &= \hat{A}_3 k^2 + \tilde{A}_3 \\ \hat{A}_3 &= -(g_w^* + \nu\psi) \\ \tilde{A}_3 &= f_u^* g_w^* - g_u^* f_w^* \end{aligned} \tag{9}$$

Let us now focus on the occurrence of the so-called wave instability, namely the destabilization of a spatially-uniform steady state via a perturbation with a non-null wavenumber k giving rise to oscillatory in time and periodic in space patterns.

To this aim, we analyse first the local stability under an homogeneous perturbation ($k = 0$). In this case, the characteristic Eq. (8) can be factorized and its solutions are:

$$\omega_1 = -\frac{1}{\tau} < 0, \quad \omega_{2,3} = \frac{1}{2} \left(f_u^* + g_w^* \pm \sqrt{(f_u^* + g_w^*)^2 - 4(f_u^* g_w^* - f_w^* g_u^*)} \right) \tag{10}$$

so that U^* is stable with respect to homogeneous perturbation iff:

$$f_u^* + g_w^* < 0, \quad f_u^* g_w^* - f_w^* g_u^* > 0. \tag{11}$$

Therefore, in the abovementioned range of parameters, $B \in (0, 2)$ and $A > 2B$, it can be easily proved that the desert state U_D^* and the vegetated one U_S^* are stable against homogeneous perturbations, whereas the vegetated state U_L^* is always unstable. Thus, this latter one cannot give rise to pattern formation and it will not be further considered in our analysis. On the other hand, taking into account non-homogeneous perturbations around the desert state U_D^* , the dispersion relation can be factorized and its solutions are given by:

$$\begin{aligned} \omega_1 &= -1 + i\nu k \\ \omega_{2,3} &= \frac{1}{2} \left(-B - \frac{1}{\tau} + i\psi k \pm \sqrt{\left(B - \frac{1}{\tau}\right)^2 - k^2 \left(\frac{4}{\tau} + \psi\right)^2 + 2i\psi k \left(\frac{1}{\tau} - B\right)} \right). \end{aligned} \tag{12}$$

Consequently, U_D^* is always stable under both homogeneous and non-homogeneous perturbations, being the real parts of all eigenvalues negative $\forall k$.

Thus, the only homogeneously-vegetated state configuration that can give rise to oscillatory periodic patterns is U_S^* . In particular, looking for solutions of the dispersion relation (8) with $\text{Re}\{\omega\} = 0$ and $\text{Im}\{\omega\} \neq 0$ for some $k \neq 0$, setting to zero the real and imaginary parts and combining the resulting equations, the critical wavenumber at the onset of instability is ruled by:

$$\theta_1 k^6 + \theta_2 k^4 + \theta_3 k^2 + \theta_4 = 0 \tag{13}$$

where

$$\begin{aligned} \theta_1 &= A_1 \beta_1^2 + \beta_1 \beta_3 [\tau(\nu f_u^* + \psi g_w^*) - (\nu + \psi)] - \beta_3^2 \hat{A}_3, \\ \theta_2 &= 2\beta_1 \beta_2 A_1 + (\beta_1 \beta_4 + \beta_2 \beta_3) [\tau(\nu f_u^* + \psi g_w^*) - (\nu + \psi)] - 2\beta_3 \beta_4 \hat{A}_3 - \beta_3^2 \tilde{A}_3, \\ \theta_3 &= A_1 \beta_2^2 + \beta_2 \beta_4 [\tau(\nu f_u^* + \psi g_w^*) - (\nu + \psi)] - \hat{A}_3 \beta_4^2 - 2\tilde{A}_3 \beta_3 \beta_4, \\ \theta_4 &= -\beta_4^2 \tilde{A}_3, \\ \beta_1 &= -\tau^2 \hat{A}_3 (\nu g_w^* + \psi f_u^*) - \nu A_1^2, \\ \beta_2 &= -\tau^2 \tilde{A}_3 (\nu g_w^* + \psi f_u^*) + A_1^2 (\nu f_u^* + \psi g_w^*), \\ \beta_3 &= A_1 [\tau f_u^* - 1 - \tau^2 \nu \psi (f_u^* + g_w^*) - \tau^2 (f_u^* \psi + g_w^* \nu) [\tau(\nu f_u^* + \psi g_w^*) - (\nu + \psi)], \\ \beta_4 &= \tau A_1 \tilde{A}_3 - A_1^2 \tilde{A}_2. \end{aligned} \tag{14}$$

The locus at which wave instability occurs may be obtained by imposing that the cubic Eq. (13) in k^2 admits three real roots, two of which are equal to each other, positive and representative of the critical squared wavenumber k_c^2 . Consequently, the wave bifurcation locus is implicitly defined by:

$$27\theta_4^2 \theta_1^2 - \theta_3^2 \theta_2^2 + 4\theta_3^3 \theta_1 + 4\theta_4 \theta_2^3 - 18\theta_4 \theta_3 \theta_2 \theta_1 = 0. \tag{15}$$

Note that, for $\tau \rightarrow 0$, the wave bifurcation locus (15) here obtained reduces to the one found in the parabolic model (Consolo and Valenti, 2019). Unfortunately, due to the highly nonlinear dependence of (15) on the plant loss B , information can be extracted from numerical investigations only.

In Fig. 1 the loci of wave instability (15) are depicted by solid lines in the (B, A) parameter plane for different inertial times $\tau \in [1, 100]$, fixing $\nu = 182.5$ and $\psi = 1$. For comparison, in the same figure the parabolic locus is also shown (red circles), pointing out a close agreement with the one obtained in the hyperbolic model for small inertial times $\tau \leq 1$.

On the other hand, by moving away from the parabolic limit, the locus of wave instability shifts up so enlarging the region where oscillatory periodic patterns may be observed, in line with our previous results (Consolo et al., 2017; Curró and Valenti, 2021; Consolo et al., 2022). To confirm this theoretical prediction, let us consider the point $P_1 = (0.38, 2.8)$ in the parameter plane (see top inset in Fig. 1) and inspect the wavenumber dependence of real and imaginary parts of the roots of the characteristic equation as the inertial time is varied. Results shown in Fig. 2(a) reveal that for $\tau = 10$, the real part of the largest eigenvalue is always negative so proving that P_1 lies outside the wave instability region. On the other hand, for $\tau = 20$ and $\tau = 100$, the existence of ranges of unstable wavenumbers confirm the upward shift of the locus of wave instability that has led P_1 to fall within the instability region (see Fig. 2(b),(c)).

Additional numerical investigations are also performed to better understand the roles of inertial time τ and advection speeds ψ and ν on the bifurcation threshold B_c . In particular, results shown in Fig. 3(a) are obtained for a fixed value of $\psi = 1$ whereas those depicted in Fig. 3(b) correspond to the case $\nu = 182.5$. In detail, for a fixed value of secondary seed dispersal and independently of the inertial time, the decrease of water advection speed leads to an increase of the critical value of the control parameter which in turn represents a reduction of the instability region (see Fig. 3(a)). This result agrees with the theoretical expectation that the formation of oscillatory patterns requires a non-null water advection speed. On the other hand, for a fixed value of water advection speed, the behaviour of the instability threshold depends on the distance from the parabolic limit. Indeed, as depicted in Fig. 3(b), for $\tau \lesssim 10^{-1}$, the critical value of control parameter is almost unaffected by the strength of secondary seed dispersal. On the contrary, far away from the parabolic limit, the role of seeds advection speed becomes more relevant. In fact, as the parameter ψ decreases, the wave instability region enlarges.

Let us now inspect the properties exhibited by oscillatory patterns by moving along the wave bifurcation locus. To this aim, let us fix three

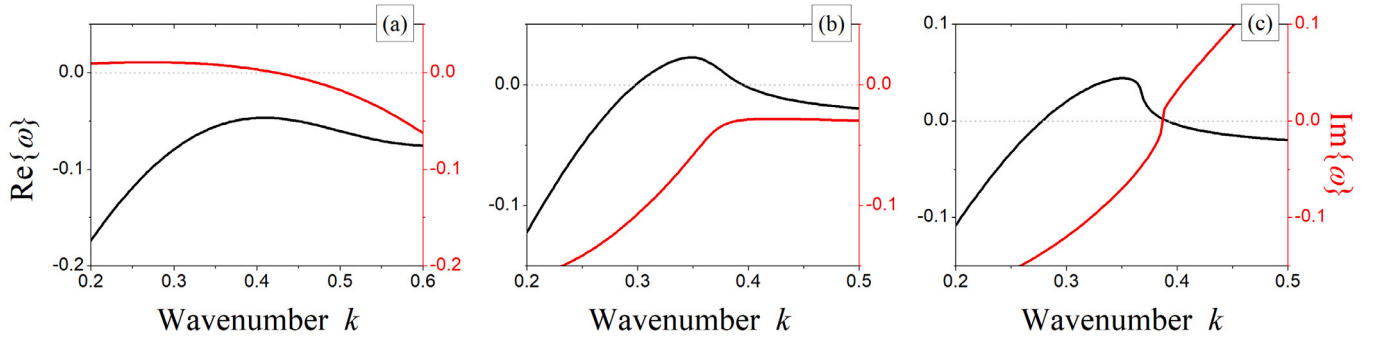


Fig. 2. Wavenumber dependence of the real (black lines) and imaginary (red lines) part of largest root of (8) evaluated at $P_1 = (0.38, 2.8)$ indicated in the top inset of Fig. 1, for different inertial times: (a) $\tau = 10$, (b) $\tau = 20$ and (c) $\tau = 100$.

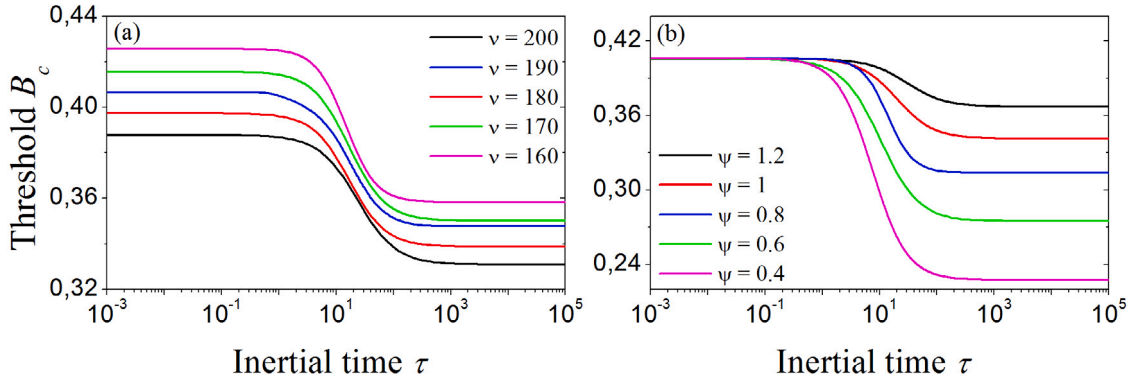


Fig. 3. Inertial time dependence of the wave instability threshold obtained for $A = 2.8$, (a) $\psi = 1$ and (b) $\nu = 182.5$.

different points on the locus obtained for $\tau = 10$ as shown in the bottom inset of Fig. 1 and precisely: $P_2 = (0.244, 1.5)$, $P_3 = (0.270, 1.7)$ and $P_4 = (0.293, 1.9)$. For these points, the wavenumber dependence of the most unstable mode at onset, characterized by angular frequency ω_c and critical wavenumber k_c , is tracked in Fig. 4. Since the imaginary part determines the modulus and direction of pattern speed $s = -\text{Im}\{\omega_c\}/k_c$, uphill (downhill) motion is observed for $\text{Im}\{\omega_c\} < 0$ ($\text{Im}\{\omega_c\} > 0$) whereas stationary patterns originate for $\text{Im}\{\omega_c\} = 0$. Theoretical predictions reveal that downhill motion takes place at the point P_2 (see Fig. 4(a)), whereas patterns become stationary at P_3 (see Fig. 4(b)) and move uphill at P_4 (see Fig. 4(c)). To check the validity of the above results, the governing system (3), (4) is integrated numerically by means of COMSOL Multiphysics® (COMSOL Multiphysics) in the computational domain $x \in [0, 200]$ over the time window $t \in [0, 200]$. Moreover, periodic boundary conditions are used and a small perturbation of the steady state U_S^* is taken as initial condition, namely patterns originating from degradation of homogeneous vegetation are here considered (Consolo and Valenti, 2019; Sherratt, 2015). Results of numerical simulations confirm our predictions, as shown in Fig. 5.

The above theoretical results are in line with some body of literature (Klausmeier, 1999; Esteban and Fairén, 2006), which predicts that vegetation groves move upslope as a result of a larger availability of moisture in the upslope margin of the band. Moreover, the presence of downslope seed transport offers a stabilizing mechanism that reduces the bands migration speed and can even reverse the direction of propagation (Saco et al., 2007; Thompson et al., 2008, 2014). However, the occurrence of upslope and downslope migration of bands is still under debate due to some controversial field evidences (Thompson et al., 2008; Tongway, 2001; Dunkerley, 2018). In particular, theoretical observations of downhill movement of bands are sometimes interpreted as a regime in which pattern migration is, instead, precluded (Thompson et al., 2008). This issue will be investigated in more detail later on in the manuscript.

According to such ecological considerations, let us describe more accurately the occurrence of stationary patterns in a framework enclosing advective terms. To this aim, let us look for solutions of the dispersion relation (8) characterized by:

$$\begin{cases} \omega = 0 \\ \frac{\partial \text{Re}\{\omega\}}{\partial k} = 0 \end{cases} \quad (16)$$

These constraints lead to the following system that defines a Turing point in the (B, A) -plane and the critical wavenumber k_c at which such an instability occurs:

$$\begin{cases} k_c = \sqrt{\frac{\nu f_u^* + \psi g_w^*}{\nu}} \\ \nu (f_u^* g_w^* - f_w^* g_u^*) - (\nu f_u^* + \psi g_w^*) (\nu \psi + g_w^*) = 0 \\ (g_w^* + \nu \psi) [(1 - \tau \nu \psi) (\nu f_u^* + \psi g_w^*) + \tau \nu (f_u^* g_w^* - f_w^* g_u^*) - \nu (f_u^* + g_w^*)] \\ + \nu (\nu f_u^* + \psi g_w^*) [\tau (\nu f_u^* + \psi g_w^*) - (\nu + \psi)] = 0 \end{cases} \quad (17)$$

As it can be noticed, the existence condition arising from (17)₁ implies a restriction on the upper limit of seed advection speed

$$\psi \leq \frac{B\nu}{1 + u_S^2} \quad (18)$$

Moreover, (17)₃ encloses the dependence of the Turing point on hyperbolicity. Indeed, by varying the inertial time, the occurrence of stationary patterns takes place at different points in the (B, A) -plane, as represented by the stars in Fig. 1. In particular, decreasing the inertial time, the Turing point moves upward along the bifurcation locus, so enlarging the range in which downhill motion is observed. Notice that, for $\tau = 1$ no star is shown since it is out of the meaningful ecological range. To describe the inertial time dependence of the Turing point B_c^T , we solve system (17) for fixed values of ν and ψ . Results are shown in Fig. 6 where the function that best approximates data is also depicted.

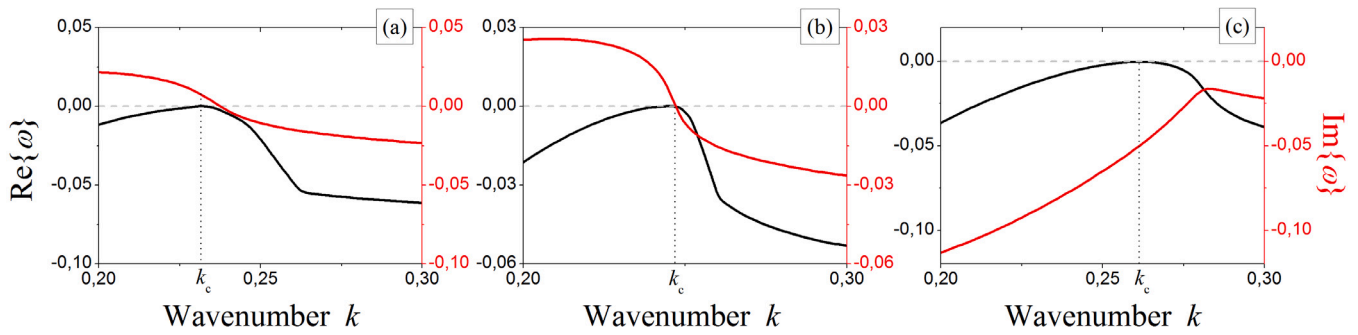


Fig. 4. Wavenumber dependence of the real (black lines) and imaginary (red lines) part of largest root of (8) evaluated at the points P_2 (a), P_3 (b) and P_4 (c) indicated in Fig. 1 for $\tau = 10$.

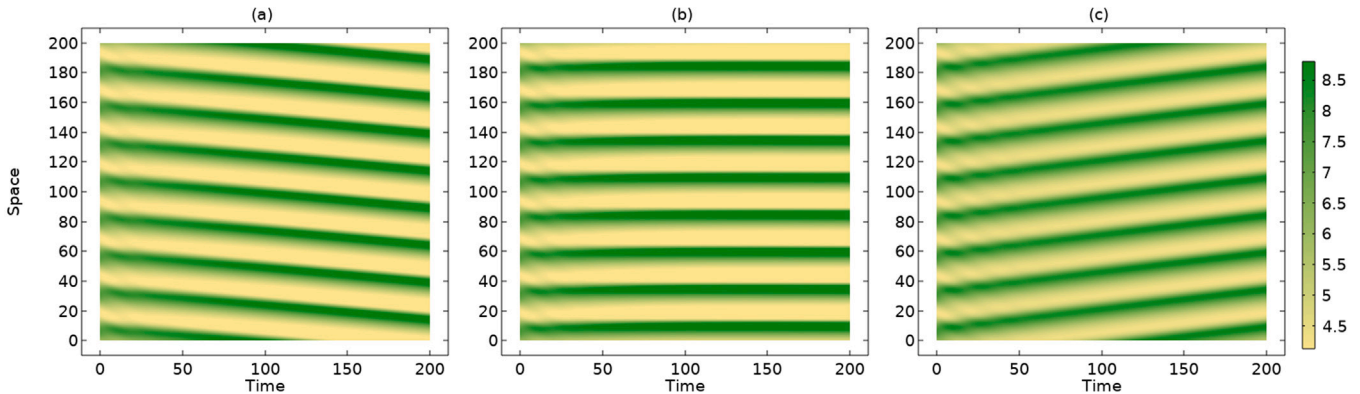


Fig. 5. Spatio-temporal dynamics of vegetation biomass $u(x,t)$ obtained by integrating numerically the governing system (3)–(4) by using the parameters associated to the panels reported in Fig. 4.

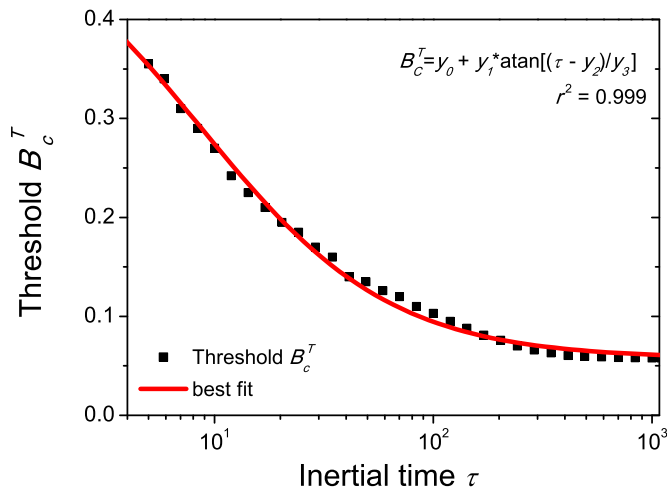


Fig. 6. Turing threshold B_c^T dependence on the inertial time τ . Black squares represent analytical results, whereas red line denotes the best fit. Fixed parameters: $\nu = 182.5$ and $\psi = 1$. Parameters appearing in the best fit function: $y_0 = 25.15$, $y_1 = -15.97$, $y_2 = -8.68$ and $y_3 = 0.25$.

Finally, let us report some quantitative field estimations of migration speeds of vegetation patches extracted from Table 12.2 in Tongway (2001) and Dunkerley (2018), which gather experimental results from several arid regions. Those data pointed out that dynamics in sloped terrains range from the quasi-stationary case, corresponding to almost null migration speed, as observed in Mexico (Montaña, 1992), Mali (Leprun, 1992), Somalia (Boaler and Hodge, 1964) and Australia (Dunkerley,

2018), to uphill motion with speed up to a 1.5 m/year, as in Mexico (Montaña, 1992), Mali (Leprun, 1992) and Sudan (Worral, 1959). To address a direct comparison with such data, let us recast the dimensionless migration speed s and the time t in the original dimensional variables S [m/year] and T [year], respectively. By using the numerical estimates of the ecological parameters provided by Klausmeier in Klausmeier (1999), we get: migration speed $S = 2s$ [m/year] and time $\tilde{T} = t/4$ [year]. Note that, the inertial time τ scales with the same law as t , i.e. $T = \tau/4$. Then, the dependence of $S(T)$ is reported in Fig. 7 for different values of ν and ψ . Results in panel (a) reveal that, for a fixed value of ν and for small values of inertial times, pattern speed S changes progressively sign from positive to negative as the seed advection speed ψ increases. On the contrary, for large values of inertial times, migration speed keeps positive and approaches asymptotically the null value far away from the parabolic limit. This behaviour holds independently of the value of the water advection speed, as proven in Fig. 7(b), which is obtained for $\psi = 1$ and variable ν . These intriguing results allow to claim that the hyperbolic model may provide satisfying interpretations of ecological observations both when patterns migrate uphill (Tongway, 2001) and when they are believed to be stationary (Dunkerley, 2018). Indeed, in the former case, the theoretically-predicted maximum speed value, about 1.2 m/year, is in close agreement with the experimental one 1.5 m/year (reported in Sudan, Tongway (2001) and Worral (1959)) for $\psi < 1$. This result suggests that the uphill migration of patterns might be associated with a very small percentage of seed advection, an increase of which would lead to the opposite behaviour. In the latter case, the vanishing migration speeds obtained for large values of inertial time yield patterns to behave as they were almost stationary, independently of the strength of secondary seed dispersal. On the other hand, close to the parabolic limit, the agreement with field data would require to set both an upper bound (18), to exclude the occurrence of downhill

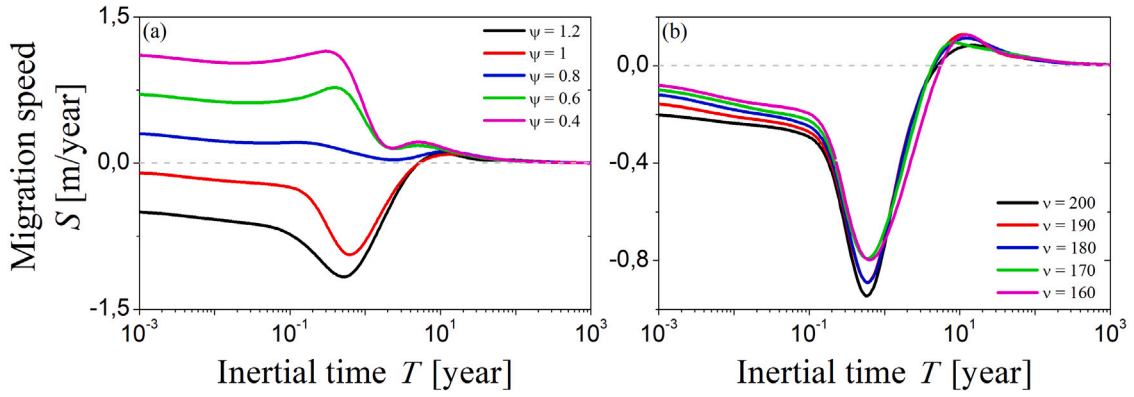


Fig. 7. Migration speed S at onset of instability ($B = B_c$) as a function of the inertial time T for different values of ψ (a) and ν (b). In (a) the water advection speed is set as $\nu = 182.5$ whereas in (b) the seed advection speed is fixed at $\psi = 1$.

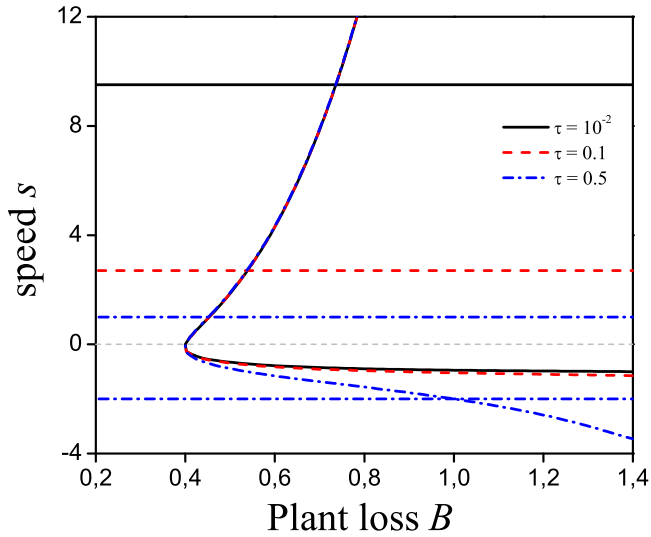


Fig. 8. Loci of Hopf bifurcation in the (B, s) parameter plane for different values of inertial time τ . Horizontal lines denote the constraints arising from Eq. (23). Fixed parameters: $\nu = 182.5$, $\psi = 1$ and $A = 2.8$.

migration (Thompson et al., 2008), and a lower bound, to prevent propagation speed to achieve very large values.

4. Periodic travelling waves

The analyses carried out in the previous sections have shed some light on the role played by inertial time and advection terms in the mechanism of formation of oscillatory periodic patterns. In this section, let us focus in more detail on the characterization of the pattern speed s in the proposed hyperbolic model (3)–(4). For this reason, we look for solutions of the governing system in the form of periodic travelling waves, namely $\mathbf{U}(x, t) = \mathbf{U}(z)$ with $z = x - st$. This leads to recast the original PDEs system in terms of the following ODEs one:

$$(M - sI) \frac{d\mathbf{U}}{dz} = \mathbf{N}(\mathbf{U}) \quad (19)$$

It is trivial to notice that (19) admits the same three steady states (5). Moreover, since we are interested in the occurrence of wave instability, we focus our analysis on the homogeneously vegetated state \mathbf{U}_S^* only. Therefore, searching for solutions in the form of $\mathbf{U} = \mathbf{U}_S^* + \hat{\mathbf{U}} \exp(\omega z)$, the following cubic characteristic equation with real coefficients is obtained:

$$\omega^3 + D_1 \omega^2 + D_2 \omega + D_3 = 0 \quad (20)$$

where

$$\begin{aligned} D_1 &= \frac{-s^2 A_1 + s[\tau(\nu f_u^* + \psi g_w^*) - (\nu + \psi)] + \hat{A}_3}{(\nu + s)(\tau s^2 + \tau \psi s - 1)}, \\ D_2 &= \frac{s \tilde{A}_2 - (\nu f_u^* + \psi g_w^*)}{(\nu + s)(\tau s^2 + \tau \psi s - 1)}, \\ D_3 &= -\frac{\tilde{A}_3}{(\nu + s)(\tau s^2 + \tau \psi s - 1)}. \end{aligned} \quad (21)$$

Then, Routh–Hurwitz criterion is applied to determine the local stability of \mathbf{U}_S^* , namely:

$$\text{Re}\{\omega\} < 0 \quad \forall \omega \iff D_1 > 0 \quad D_3 > 0 \quad D_1 D_2 - D_3 > 0 \quad (22)$$

The first two conditions lead to:

$$\begin{aligned} \text{(i)} \quad & \text{if } \tau f_u^* - 1 > 0 \quad \wedge \quad s_4 > s_2 \quad \Rightarrow \quad s_1 < s < \min\{s_2, s_3\} \\ \text{(ii)} \quad & \text{if } \tau f_u^* - 1 > 0 \quad \wedge \quad s_4 < s_2 \quad \Rightarrow \quad s_1 < s < s_3 \vee s_4 < s < s_2 \\ \text{(iii)} \quad & \text{if } \tau f_u^* - 1 < 0 \quad \wedge \quad s_1 > s_3 \quad \Rightarrow \quad \max\{s_1, s_4\} < s < s_2 \\ \text{(iv)} \quad & \text{if } \tau f_u^* - 1 < 0 \quad \wedge \quad s_1 < s_3 \quad \Rightarrow \quad s_1 < s < s_3 \vee s_4 < s < s_2 \end{aligned} \quad (23)$$

where

$$\begin{aligned} s_{1,2} &= \frac{1}{2} \left(-\psi \mp \sqrt{\psi^2 + 4/\tau} \right), \\ s_{3,4} &= \frac{1}{2A_1} \left[\tau(\nu f_u^* + \psi g_w^*) - (\nu + \psi) \right. \\ & \quad \left. \mp \sqrt{[\tau(\nu f_u^* + \psi g_w^*) - (\nu + \psi)]^2 + 4A_1 \hat{A}_3} \right]. \end{aligned} \quad (24)$$

Note that (23) represents the restrictions provided by the hyperbolic nature of the model that, as expected, imposes the speed of propagation to be limited. Indeed, in the parabolic limit $\tau \rightarrow 0$, the previous conditions reduce to:

$$\begin{cases} s < \bar{s}_3 \quad \vee \quad s > \bar{s}_4 \\ [s^2 + (\psi + \nu)s + \psi\nu + g_w^*] [(g_w^* + f_u^*)s + \psi g_w^* + \nu f_u^*] \\ -(s + \nu)(f_u^* g_w^* - f_w^* g_u^*) > 0 \end{cases} \quad (25)$$

where

$$\bar{s}_{3,4} = -\frac{1}{2} \left[\psi + \nu \pm \sqrt{(\psi - \nu)^2 - 4g_w^*} \right] \quad (26)$$

which highlight the absence of an upper limit, so allowing the possibility to achieve the paradox of an infinite propagation speed.

On the other hand, violation of the last condition in (22) defines the locus of Hopf bifurcation:

$$\begin{aligned} \left\{ -s^2 A_1 + s[\tau(\nu f_u^* + \psi g_w^*) - (\nu + \psi)] + \hat{A}_3 \right\} \left[s \tilde{A}_2 - (\nu f_u^* + \psi g_w^*) \right] \\ + \tilde{A}_3 (\nu + \psi) (\tau s^2 + \tau \psi s - 1) = 0. \end{aligned} \quad (27)$$

As known (Sherratt, 2010; Sherratt and Lord, 2007; Sherratt, 2011), the occurrence of Hopf bifurcation at \mathbf{U}_S^* to a small amplitude periodic

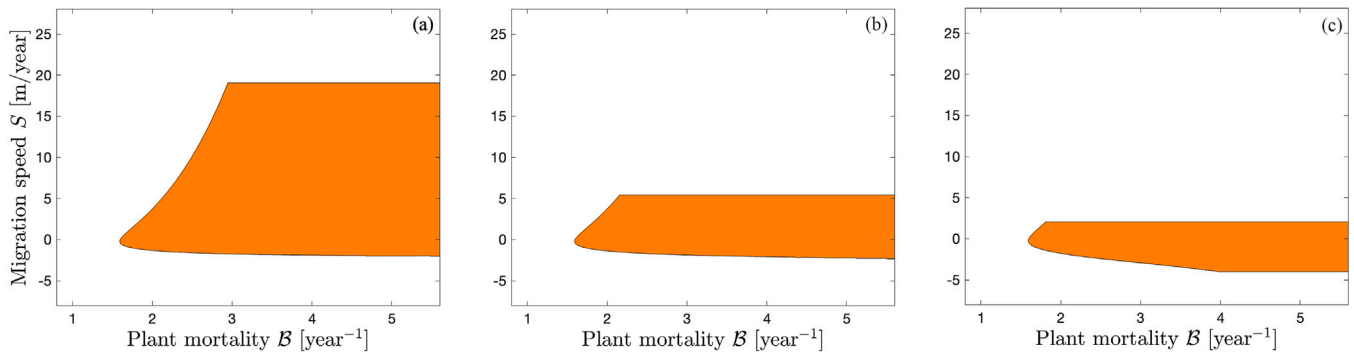


Fig. 9. Stability regions for travelling waves in the (B, S) plane as the inertial time is varied: (a) $\tau = 10^{-2}$, (b) $\tau = 0.1$ and (c) $\tau = 0.5$.

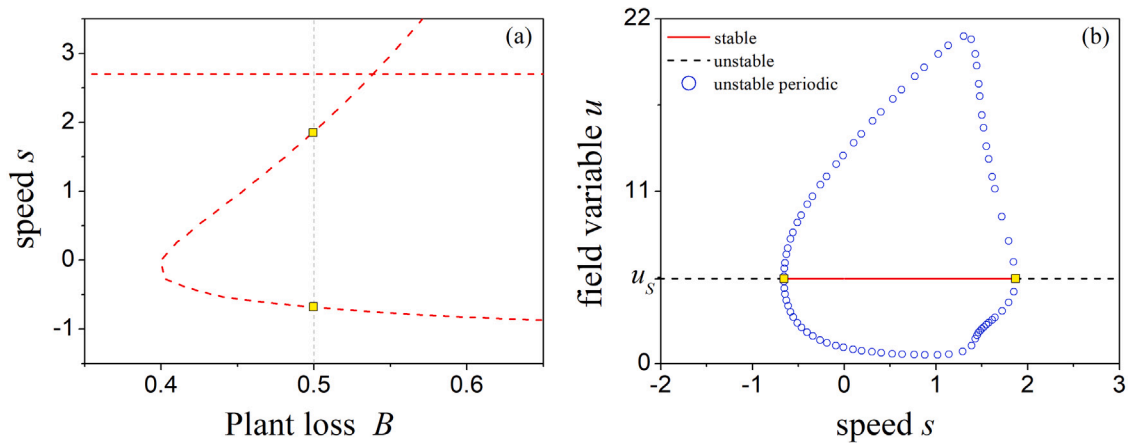


Fig. 10. (a) Locus of Hopf bifurcation in the (B, s) plane for $\tau = 0.1$. (b) The corresponding bifurcation diagram obtained for $B = 0.5$. The parameter set is the same as the one used in Fig. 8.

solution of the ODEs system (19) corresponds to a travelling wave solution of the PDEs system (3)–(4).

Unfortunately, due to the highly nonlinear structure of the implicit locus (27) on the plant loss B , information can only be extracted numerically. Outcomes of this analysis are shown in Fig. 8 where the locus of Hopf bifurcation is depicted for different values of the inertial time τ , considering $v = 182.5$, $\psi = 1$ and $A = 2.8$. This parameter set falls into setup (iii) of (23). In the same figure, the horizontal lines represent the constraints $s = s_1$ and $s = s_2$, whereas the condition $s = s_4$ is not depicted as it always lies below the Hopf locus and brings no contribution. Considering the whole restrictions, the stability region varies with the inertial times as shown in Fig. 9, where all the quantities have been recast in the original dimensional variables (according to Klausmeier (1999), the plant mortality B is related to the dimensionless one by $B = 4B$). As it can be noticed, despite larger values of inertial times enlarge the region defined by the Hopf locus (as one can argue from Fig. 8), they progressively restrict the set of allowed speed, according to the stability conditions (23)(iii), as depicted by the coloured areas in Fig. 9.

Finally, to gain more insights into this phenomenon, we fix the inertial time at $\tau = 0.1$ and compare the theoretical predictions (23)(iii), (27) with the numerical ones extracted from the bifurcation diagram obtained for $B = 0.5$ and built by the XPPAUT tool (Ermentrout, 2002). Results are shown in Fig. 10. In both panels of this figure, the yellow squares define the upper and lower bounds of the admitted wave speed within which the limit cycle (represented by blue circles in the right panel) is observed. As it can be noticed, the excellent agreement here obtained provides a further confirmation of the analysis here carried out.

All the above described results fully agree with the ones depicted in Fig. 7 and point out that, moving far away from the parabolic limit, pattern dynamics becomes almost stationary. Interestingly, by direct comparison with field data, our findings might, in turn, provide a strategy to estimate the order of magnitude of inertial effects taking place in dryland vegetation dynamics.

5. Conclusions

In this manuscript we propose a twofold generalization of the Klausmeier model, that is one of the easiest tools used to describe the formation of vegetation stripes along the slopes of semi-arid environments. Compared to the original parabolic model (Klausmeier, 1999), the one here discussed also accounts for: (i) secondary dispersal of seeds, through an additional advection term (Consolo and Valenti, 2019) and (ii) inertial effects on the vegetation component, which lead to build up a hyperbolic framework (Barbera et al., 2015). Patterned vegetation dynamics are analysed by means of linear stability analysis in order to deduce and characterize the locus of wave instability as a function of all the model parameters. Moreover, additional information on the pattern speed are extracted by means of periodic travelling waves. Theoretical predictions, which are complemented by numerical simulations, allow to draw several conclusions.

First, the pattern-forming region enlarges (reduces) as the inertial time (seed advection speed) increases, as depicted in Figs. 1 and 3. Therefore, the presence of inertia does not only affect transient dynamics, as expected, but also plays an active role in allowing pattern dynamics to be observed over a wider range of model parameters.

Moreover, the proposed hyperbolic generalization of the Klausmeier model may provide a satisfying description of experimental data for

both migrating and stationary patterns. Indeed, close to the parabolic limit, the model allows to reproduce both directions of pattern propagation as a function of seed advection speed, as shown in Figs. 4–7. On the contrary, far from the parabolic limit and independently of secondary seed dispersal, the theoretically-predicted migration speed approaches the zero value so mimicking the regime of quasi-stationary patterns. The constraints on the allowed wave speed arising from the hyperbolic nature of the model are particularly tangible in Figs. 8,9, where the stability region of travelling waves progressively shrinks as the inertial time is increased.

Finally, we believe that the results here obtained might shed some light on the current debate on the mechanisms responsible for the effective migration on vegetation bands along slopes of arid terrains. At the same time, while we are aware of the huge difficulties encountered in addressing such a long-term experimental field observations, a larger and more accurate availability of field data might provide an indirect estimation of the order of magnitude of plant inertia.

CRediT authorship contribution statement

Giancarlo Consolo: Conceptualization, Formal analysis, Investigation, Writing – original draft, Writing – review & editing, Supervision, Funding acquisition. **Gabriele Grifó:** Software, Formal analysis, Investigation, Writing – original draft, Funding acquisition. **Giovanna Valenti:** Conceptualization, methodology, Formal analysis, Investigation, Writing – original draft, Writing – review & editing, Supervision, Funding acquisition.

Declaration of competing interest

The authors declare that they have no known competing financial interests or personal relationships that could have appeared to influence the work reported in this paper.

Data availability

No data was used for the research described in the article.

Acknowledgements

This research was funded by MUR (Italian Ministry of University and Research) through project PRIN2017 no. 2017YBKNCCE, “Multi-scale phenomena in Continuum Mechanics: singular limits, off-equilibrium and transitions” and by INdAM-GNFM. Gabriele Grifó also acknowledges support from INdAM-GNFM through “Progetto Giovani GNFM 2020” entitled “Analisi di biforcazione e teoremi di buona posizione in modelli matematici multi-scala di interesse”.

References

- AI-Ghoul, M., Eu, B.C., 1996. Hyperbolic reaction–diffusion equations and irreversible thermodynamics: Cubic reversible reaction model. *Physica D* 90, 119–153. [http://dx.doi.org/10.1016/0167-2789\(95\)00231-6](http://dx.doi.org/10.1016/0167-2789(95)00231-6).
- Barbera, E., et al., 2015. On discontinuous travelling wave solutions for a class of hyperbolic reaction–diffusion models. *Physica D* 308, 116–126. <http://dx.doi.org/10.1016/j.physd.2015.06.011>.
- Bastiaansen, R., Carter, P., Doelman, A., 2019. Stable planar vegetation stripe patterns on sloped terrain in dryland ecosystems. *Nonlinearity* 32 (8), 2759. <http://dx.doi.org/10.1088/1361-6544/ab1767>.
- Boaler, S.B., Hodge, C.A.H., 1964. Observations on vegetation arcs in the northern region Somali Republic. *J. Ecol.* 52, 511–544. <http://dx.doi.org/10.2307/2257847>.
- Borgogno, F., et al., 2009. Mathematical models of vegetation pattern formation in ecophysiology. *Rev. Geophys.* 47, RG1005. <http://dx.doi.org/10.1029/2007RG000256>.
- Brown, J.H., et al., 2001. Complex species interactions and the dynamics of ecological systems: long-term experiments. *Science* 293, 643–650. <http://dx.doi.org/10.1126/science.293.5530.643>.
- COMSOL Multiphysics® V. 6.0. COMSOL AB Stockholm, Sweden www.comsol.com.

- Consolo, G., Grifó, G., 2022. Eckhaus instability of stationary patterns in hyperbolic reaction–diffusion models on large finite domains. *Part. Diff. Eq. Appl.* 3, 57. <http://dx.doi.org/10.1007/s42985-022-00193-0>.
- Consolo, G., Valenti, G., 2019. Secondary seed dispersal in the Klausmeier model of vegetation for sloped semi-arid environments. *Ecol. Model.* 402, 66–75. <http://dx.doi.org/10.1016/j.ecolmodel.2019.02.009>.
- Consolo, G., et al., 2017. Pattern formation and modulation in a hyperbolic vegetation model for semiarid environments. *Appl. Math. Model.* 43, 372–392. <http://dx.doi.org/10.1016/j.apm.2016.11.031>.
- Consolo, G., et al., 2019. Supercritical and subcritical Turing pattern formation in a hyperbolic vegetation model for flat arid environments. *Physica D* 398, 141–163. <http://dx.doi.org/10.1016/j.physd.2019.03.006>.
- Consolo, G., et al., 2020. Turing vegetation patterns in a generalized hyperbolic Klausmeier model. *Math. Methods Appl. Sci.* 43, 10474–10489. <http://dx.doi.org/10.1002/mma.6518>.
- Consolo, G., et al., 2022. Oscillatory periodic pattern dynamics in hyperbolic reaction–advection–diffusion models. *Phys. Rev. E* 105, 034206. <http://dx.doi.org/10.1103/PhysRevE.105.034206>.
- Curró, C., Valenti, G., 2021. Pattern formation in hyperbolic models with cross-diffusion: Theory and applications. *Physica D* 418, 132846. <http://dx.doi.org/10.1016/j.physd.2021.132846>.
- Deblauwe, V., et al., 2011. Environmental modulation of self-organized periodic vegetation patterns in Sudan. *Ecography* 34, 990–1001. <http://dx.doi.org/10.1111/j.1600-0587.2010.06694>.
- Deblauwe, V., et al., 2012. Determinants and dynamics of banded vegetation pattern migration in arid climates. *Ecol. Monogr.* 82, 3–21. <http://dx.doi.org/10.1890/11-0362.1>.
- Dunkerley, D., 2018. Banded vegetation in some Australian semi-arid landscapes: 20 years of field observations to support the development and evaluation of numerical models of vegetation pattern evolution. *Desert* 23, 165–187.
- Eigentler, L., Sherratt, J.A., 2020. An integrodifference model for vegetation patterns in semi-arid environments with seasonality. *J. Math. Biol.* 81, 875–904. <http://dx.doi.org/10.1007/s00285-020-01530-w>.
- Ermentrout, B., 2002. Simulating, Analyzing, and Animating Dynamical Systems. SIAM, <http://dx.doi.org/10.1137/1.9780898718195>.
- Esteban, J., Fairén, V., 2006. Self-organized formation of banded vegetation patterns in semi-arid regions: A model. *Ecol. Complex.* 3, 109–118. <http://dx.doi.org/10.1016/j.ecocom.2005.10.001>.
- Gandhi, P., et al., 2018. A topographic mechanism for arcing of dryland vegetation bands. *J. R. Soc. Interface* 15 (147), 20180508. <http://dx.doi.org/10.1098/rsif.2018.0508>.
- García-Fayos, P., Gasque, M., 2002. Consequences of a severe drought on spatial patterns of woody plants in a two-phase mosaic steppe of *Stipa tenacissima*. *J. Arid Environ.* 52, 199–208. <http://dx.doi.org/10.1006/jare.2002.0987>.
- Gilad, E., et al., 2004. Ecosystem engineers: From pattern formation to habitat creation. *Phys. Rev. Lett.* 93, 098105. <http://dx.doi.org/10.1103/PhysRevLett.93.098105>.
- Gowda, K., et al., 2018. Signatures of human impact on self-organized vegetation in the Horn of Africa. *Sci. Rep.* 8, 3622. <http://dx.doi.org/10.1038/s41598-018-22075-5>.
- Hillen, T., 2002. Hyperbolic models for chemosensitive movement. *Math. Models Methods Appl. Sci.* 12, 1–28. <http://dx.doi.org/10.1142/S0218202502002008>.
- Hillerislambers, R., et al., 2001. Vegetation pattern formation in semi-arid grazing systems. *Ecology* 82, 50–61. [http://dx.doi.org/10.1890/0012-9658\(2001\)082\[0050:VPFISA\]2.0.CO;2](http://dx.doi.org/10.1890/0012-9658(2001)082[0050:VPFISA]2.0.CO;2).
- Klausmeier, C.A., 1999. Regular and irregular patterns in semiarid vegetation. *Science* 284, 1826–1828. <http://dx.doi.org/10.1126/science.284.5421.1826>.
- Langevelde, F., 2016. Soil seed bank dynamics under the influence of grazing as alternative explanation for herbaceous vegetation transitions in semi-arid rangelands. *Ecol. Model.* 337, 253–261. <http://dx.doi.org/10.1016/j.ecolmodel.2016.07.013>.
- Leprun, J.C., 1992. Etude de Quelques Brousses Tigrés Sahéliennes: Structure, Dynamique, Écologie, de l'ORSTOM L'aridité, une contrainte au développement, Paris, pp. 221–224.
- Marasco, A., et al., 2014. Vegetation pattern formation due to interactions between water availability and toxicity in plant?soil feedback. *Bull. Math. Biol.* 76 (11), 2866–2883. <http://dx.doi.org/10.1007/s11538-014-0036-6>.
- Mendez, V., et al., 2010. Reaction-Transport Systems. Springer-Verlag, Berlin Heidelberg, <http://dx.doi.org/10.1007/978-3-642-11443-4>.
- Meron, E., 2015. Nonlinear Physics of Ecosystems. CRC Press, Boca Raton, <http://dx.doi.org/10.1063/PT.3.2949>.
- Meron, E., 2018. From patterns to function in living systems: Dryland ecosystems as a case study. *Ann. Rev. Condens. Matter Phys.* 9, 79–103. <http://dx.doi.org/10.1146/annurev-conmatphys-033117-053959>.
- Milchunas, D.G., Lauenroth, W.K., 1995. Inertia in plant community structure: state changes after cessation of nutrient-enrichment stress. *Ecol. Appl.* 5, 452–458. <http://dx.doi.org/10.2307/1942035>.
- Montaña, C., 1992. The colonisation of bare areas two-phase mosaics of an arid ecosystem. *J. Ecol.* 80, 315–327. <http://dx.doi.org/10.2307/2261014>.
- Mvogo, A., et al., 2018. Diffusive instabilities in a hyperbolic activator-inhibitor system with superdiffusion. *Phys. Rev. E* 97, 032129. <http://dx.doi.org/10.1103/PhysRevE.97.032129>.

- Pueyo, et al., 2008. Use of the modified BCR three-step sequential extraction procedure for the study of trace element dynamics in contaminated soils. *Env. Poll.* 152, 330–341. <http://dx.doi.org/10.1016/j.envpol.2007.06.020>.
- Rietkerk, M., 2002. Self-organisation of vegetation in arid ecosystems. *Am. Nat.* 160 (524), <http://dx.doi.org/10.1086/342078>.
- Rietkerk, M., et al., 2000. Multiscale soil and vegetation patchiness along a gradient of herbivore impact in a semi-arid grazing system in West Africa. *Plant Ecol.* 148, 207–224. <http://dx.doi.org/10.1023/A:1009828432690>.
- Ruggeri, T., Sugiyama, M., 2021. Classical and Relativistic Rational Extended Thermodynamics of Gases. Springer, Cham, <http://dx.doi.org/10.1007/978-3-030-59144-1>.
- Saco, P.M., et al., 2007. Eco-geomorphology of banded vegetation patterns in arid and semi-arid regions. *Hydrol. Earth Syst. Sci.* 11, 1717–1730. <http://dx.doi.org/10.1029/2008GL036044>.
- Sherratt, J.A., 2005. An analysis of vegetation stripe formation in semi-arid landscapes. *J. Math. Biol.* 51, 183–197. <http://dx.doi.org/10.1007/s00285-005-0319-5>.
- Sherratt, J.A., 2010. Pattern solutions of the Klausmeier Model for banded vegetation in semi-arid environments I. *Nonlinearity* 23, 2657–2675. <http://dx.doi.org/10.1098/rspa.2011.0194>.
- Sherratt, J.A., 2011. Pattern solutions of the Klausmeier model for banded vegetation in semi-arid environments II: patterns with the largest possible propagation speeds. *Proc. R. Soc. Lond. Ser. A Math. Phys. Eng. Sci.* 467, 3272–3294. <http://dx.doi.org/10.1098/rspa.2011.0194>.
- Sherratt, J.A., 2013. Pattern solutions of the klausmeier model for banded vegetation in semiarid environments v: The transition from patterns to desert. *SIAM J. Appl. Math.* 73, 1347–1367. <http://dx.doi.org/10.1137/120899510>.
- Sherratt, J.A., 2015. Using wavelength and slope to infer the historical origin of semiarid vegetation bands. *Proc. Natl. Acad. Sci.* 112 (4202), <http://dx.doi.org/10.1073/pnas.1420171112>.
- Sherratt, J.A., Lord, G.J., 2007. Nonlinear dynamics and pattern bifurcations in a model for vegetation stripes in semi-arid environments. *Theor. Pop. Biol.* 71, 1–11. <http://dx.doi.org/10.1016/j.tpb.2006.07.009>.
- Sherratt, J.A., Synodinos, A.D., 2012. Vegetation patterns and desertification waves in semi-arid environments: mathematical models based on local facilitation in plants. *Discrete Cont. Dyn. Syst. Ser. B* 17, 2815–2827. <http://dx.doi.org/10.3934/dcdsb.2012.17.2815>.
- Siteur, K., 2014. Beyond turing: the response of patterned ecosystems to environmental change. *Ecol. Complex.* 20, 81–96. <http://dx.doi.org/10.1016/j.ecocom.2014.09.002>.
- Sohoulane Djebou, D.C., Singh, V.P., 2015. Retrieving vegetation growth patterns from soil moisture, precipitation and temperature using maximum entropy. *Ecol. Model.* 309–310, 10–21. <http://dx.doi.org/10.1016/j.ecolmodel.2015.03.022>.
- Van der Stelt, S., et al., 2013. Rise and fall of periodic patterns for a generalized Klausmeier-Gray-Scott Model. *J. Nonlinear Sci.* 23, 39–95. <http://dx.doi.org/10.1007/s00332-012-9139-0>.
- Straughan, B., 2011. Heat waves. In: *Applied Mathematical Sciences*. Springer, New York, <http://dx.doi.org/10.1007/978-1-4614-0493-4>.
- Thompson, S., Katul, G., 2009. Secondary seed dispersal and its role in landscape organization. *Geoph. Res. Lett.* 36 (L02402), <http://dx.doi.org/10.1029/2008GL036044>.
- Thompson, S., et al., 2008. Role of biomass spread in vegetation pattern formation within arid ecosystems. *Water Resour. Res.* 44 (W10421), <http://dx.doi.org/10.1029/2008WR006916>.
- Thompson, S., et al., 2014. Secondary dispersal driven by overland flow in drylands: Review and mechanistic model development. *Mov. Ecol.* 2, 4. <http://dx.doi.org/10.1186/2051-3933-2-7>.
- Tongway, D.J., 2001. *BandEd Vegetation Patterning in Arid and Semiarid Environments*. Springer, New York, <http://dx.doi.org/10.1007/978-1-4613-0207-0>.
- Ursino, N., Rulli, M.C., 2010. Combined effect of fire and water scarcity on vegetation patterns in arid lands. *Ecol. Model.* 221, 2353–2362. <http://dx.doi.org/10.1016/j.ecolmodel.2010.06.018>.
- Valentin, C., d'Herbés, J.M., 1999. Niger tiger bush as a natural water harvesting system. *Catena* 37, 231–256. [http://dx.doi.org/10.1016/S0341-8162\(98\)00061-7](http://dx.doi.org/10.1016/S0341-8162(98)00061-7).
- Von Hardenberg, J., et al., 2001. Diversity of vegetation patterns and desertification. *Phys. Rev. Lett.* 87, 198101. <http://dx.doi.org/10.1103/PhysRevLett.87.198101>.
- Von Holle, B., et al., 2003. The importance of biological inertia in plant community resistance to invasion. *J. Veg. Sci.* 14, 425–432. <http://dx.doi.org/10.1111/j.1654-1103.2003.tb02168.x>.
- Worrall, G.A., 1959. The butanna grass pattern. *J. Soil Sci.* 10, 34–53. <http://dx.doi.org/10.1111/j.1365-2389.1959.tb00664.x>.
- Zelnik, Y.R., et al., 2017. Desertification by front propagation? *J. Theoret. Biol.* 418, 27–35. <http://dx.doi.org/10.1016/j.jtbi.2017.01.029>.
- Zemskov, E.P., Horsthemke, W., 2016. Diffusive instabilities in hyperbolic reaction-diffusion equations. *Phys. Rev. E* 93, 032211. <http://dx.doi.org/10.1103/PhysRevE.93.032211>.